

Radially-Distorted Conjugate Translations

James Pritts¹ Zuzana Kúkelová¹
 Visual Recognition Group, CTU in Prague¹

Viktor Larsson² Ondřej Chum¹
 Centre for Mathematical Sciences, Lund University²

Abstract

This paper introduces the first minimal solvers that jointly solve for affine-rectification and radial lens distortion from coplanar repeated patterns. Even with imagery from moderately distorted lenses, plane rectification using the pinhole camera model is inaccurate or invalid. The proposed solvers incorporate lens distortion into the camera model and extend accurate rectification to wide-angle imagery, which is now common from consumer cameras. The solvers are derived from constraints induced by the conjugate translations of an imaged scene plane, which are integrated with the division model for radial lens distortion. The hidden-variable trick with ideal saturation is used to reformulate the constraints so that the solvers generated by the Gröbner-basis method are stable, small and fast.

The proposed solvers are used in a RANSAC-based estimator. Rectification and lens distortion are recovered from either one conjugately translated affine-covariant feature or two independently translated similarity-covariant features. Experiments confirm that RANSAC accurately estimates the rectification and radial distortion with very few iterations. The proposed solvers are evaluated against the state-of-the-art for affine rectification and radial distortion estimation.

1. Introduction

Scene-plane rectification is used in many classic computer-vision tasks, including single-view 3D reconstruction, camera calibration, grouping coplanar symmetries, and image editing [25, 20, 15]. In particular, the affine rectification of a scene plane transforms the camera’s principal plane so that it is parallel to the scene plane. This restores the affine invariants of a scene plane, which include parallelism of lines and translational symmetries [9, 20]. There is only an affine transformation between the affine-rectified imaged scene plane and its real-world counterpart. The removal of the effects of perspective imaging is helpful to understanding the geometry of the scene plane.

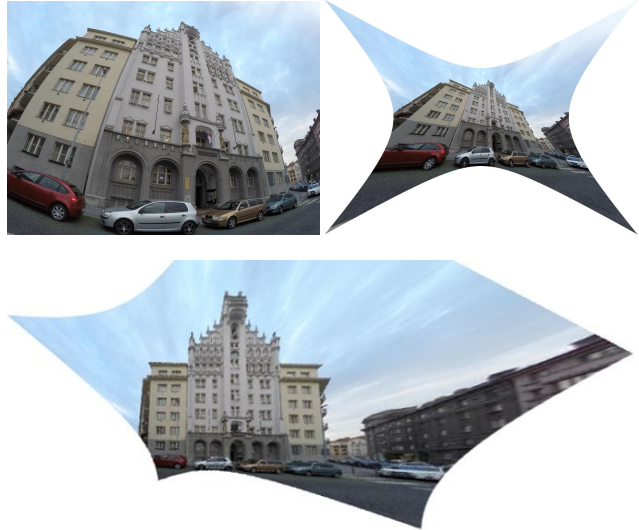


Figure 1: Input (top left) is a distorted view of a scene plane, and output (top right, bottom) are the the undistorted and rectified scene plane after undistortion. The method is fully automatic.

Wide-angle imagery that has significant lens distortion is common since consumer photography is now dominated by mobile-phone and GoPro-type cameras. High-accuracy rectification from wide-angle imagery is not possible with only pinhole camera models [11, 24]. Lens distortion can be estimated by performing a camera calibration apriori, but a fully automated method is desirable.

Several state-of-the-art planar-rectification methods assume a pinhole camera model, which ignores the effect of lens distortion [1, 4, 15, 26]. Pritts *et al.* [20] attempt to upgrade the pinhole camera model with radial lens distortion by giving an initial guess of scene-plane rectification consistent with a pinhole camera to a non-linear optimization that incorporates a lens-distortion model. However, even with relaxed thresholds, a robust estimator (*i.e.* RANSAC) will discard measurements that capture the most extreme effects of lens distortion, especially around the boundary of the image, since these measurements are not consistent with the pinhole-camera assumption. Thus, failing to account for

J. Pritts and O. Chum are supported by MSMT LL1303 ERC-CZ.



Figure 2: *GoPro* camera with varying field-of-view settings. Input images (top row) for different field-of-view settings. Undistorted and rectified results (bottom row).

lens distortion while labeling which measurements to discard as outliers, as done during RANSAC iterations, will give biased fits that underestimate the camera’s lens-distortion [11], which in turn degrades rectification accuracy.

This paper introduces the first minimal solvers that jointly solve for the affine rectification of an imaged scene plane and a camera’s radial lens distortion. The solvers are derived from constraints induced by conjugate translations of an imaged scene plane (see Sec. 2 for details), which are integrated with the division model of radial distortion [7]. Despite the simple formulation of the division model, it is accurate for even wide-angle lenses [7]. In addition, the solvers estimate the vanishing translation direction of the corresponded points used for input.

Two types of solvers are introduced: *one-direction solvers*, which require 3 coplanar point correspondences that translate in the same direction, and *two-direction solvers*, which require 4 coplanar point correspondences, 2 of which translate in one-direction and the remaining 2 in a different direction.

Fitzgibbon used a one-parameter division model to develop a minimal solver for jointly estimating lens distortion with a fundamental matrix or homography [7]. Kukelova *et al.* [11] proposed an extension to [7] for homographies to model two-views from cameras with different radial lens distortions. These two-view solvers can jointly estimate lens distortion and conjugate translations, but are overparameterized for this task, which can result in inaccurate estimates as is shown by the experiments in Sec. 5.

Related methods in single-view geometry using the division model include Wildenauer *et al.* [24] and Antunes *et al.* [2]. Both use constraints induced by imaged parallel lines to jointly solve for their vanishing point and the parameter of the division model, but both require a multi-model esti-

mation to recover scene-plane rectification (*i.e.* 2 consistent vanishing points) and an intermediate representation (either fitted circles [24] or circle centers in [2]) of the detected line as input to their solvers.

The systems of polynomial equations induced from the constraints arising from joint estimation of conjugate translation with the division-model parameter are solved using an algebraic method based on Gröbner bases. Automated solver-generators using the Gröbner basis method [10, 12] were recently used to generate solvers for several problems in multi-view geometry [10, 13, 12, 11]. However, straightforward application of an automated solver-generator to the proposed problem resulted in unstable solvers (see Sec. 5). Therefore, we transformed the constraints to simplify the structure of the systems of polynomial equations, while explicitly accounting for the parasitic solutions that arose from the new formulation. The new formulation resulted in solvers with increased stability and speed.

The problem of rectification is closely coupled with the detection of coplanar repeats in a classic chicken-and-egg problem: rectification is easy if the repeats are grouped, and repeats are easily grouped if the affine invariants of the rectified plane are available [20]. Most methods tentatively group repeats from their local texture, which is verified later by a hypothesized rectification. Methods using this approach include Schaffalitzky *et al.* [22], which, similar to the solvers proposed in this paper, uses constraints induced by conjugate translations to recover the scene-plane’s vanishing line, and Chum *et al.* [4], which uses the constraint that coplanar repeats are equiareal in the scene-plane’s affine-rectified image. None of these methods account for lens distortion, and do not perform well on wide-angle imagery (see Sec. 5).

Covariant feature detectors are used to extract point correspondences [14, 16, 18, 23] needed by the solvers. In particular, only one affine-covariant feature correspondence is used to generate the 3 point correspondences needed for the one-direction solvers, or two similarity-covariant feature correspondences are used to generate the 4 point correspondences needed for the two-direction solvers. We incorporate the proposed solvers into a RANSAC-based framework for the joint estimation of scene-plane rectification and radial distortion and geometric grouping of repeated features. With one or two-correspondence sampling, RANSAC quickly finds a model that accurately undistorts and rectifies, even for difficult scenes.

2. Problem Formulation

Assume that the scene plane π and a camera’s image plane π' are related point-wise by the homography P , so that $\alpha_i \mathbf{x}'_i = P \mathbf{X}_i$, where α_i is a scalar, $\mathbf{X}_i \in \pi$ and $\mathbf{x}'_i \in \pi'$. Let \mathbf{X}_i and \mathbf{X}'_i be two points on the scene plane π such that $\mathbf{X}'_i - \mathbf{X}_i = \mathbf{t}$. By encoding \mathbf{t} in the homogeneous transla-

tion matrix \mathbf{T} , the points \mathbf{X}_i and \mathbf{X}'_i as imaged by camera \mathbf{P} can be expressed as

$$\alpha_i \mathbf{x}'_i = \mathbf{P} \mathbf{X}'_i = \mathbf{P} \mathbf{T} \mathbf{X}_i = \underbrace{\mathbf{P} \mathbf{T} \mathbf{P}^{-1}}_{\mathbf{H}_u} \mathbf{x}_i, \quad (1)$$

where the homography \mathbf{H}_u is called a conjugate translation because of its matrix decomposition $\mathbf{P} \mathbf{T} \mathbf{P}^{-1}$ and points \mathbf{x}_i and \mathbf{x}'_i are in correspondence with respect to the conjugate translation \mathbf{H}_u , which we denote $\mathbf{x}_i \leftrightarrow \mathbf{x}'_i$ [9, 22]. Decomposing \mathbf{H}_u into its projective components gives

$$\begin{aligned} \alpha_i \mathbf{x}'_i &= \mathbf{H}_u \mathbf{x}_i = \mathbf{P} \mathbf{I}_3 \mathbf{P}^{-1} + \mathbf{P} \begin{pmatrix} t_x \\ t_y \\ 1 \end{pmatrix} \begin{pmatrix} 0 \\ 0 \\ 1 \end{pmatrix}^\top \mathbf{x}_i \\ &= [\mathbf{I}_3 + s_i^u \mathbf{u} \mathbf{l}^\top] \cdot \mathbf{x}_i \end{aligned} \quad (2)$$

where \mathbf{I}_3 is the 3×3 identity matrix, and

- line \mathbf{l} is the scene plane’s imaged vanishing line,
- point \mathbf{u} is the vanishing direction of translation, which must meet the vanishing line \mathbf{l} , *i.e.*, $\mathbf{l}^\top \mathbf{u} = 0$,
- and scalar s_i^u is the magnitude of translation in the vanishing direction \mathbf{u} for the point correspondence $\tilde{\mathbf{x}}_i \leftrightarrow \tilde{\mathbf{x}}'_i$ [22].

Note that (2) holds only for points projected by an ideal perspective camera viewing a scene plane, which is parameterized by the homography \mathbf{P} as defined above. For every real camera, some amount of radial distortion is always present, so for (2) to hold, the measured image points $\tilde{\mathbf{x}}_i$ and $\tilde{\mathbf{x}}'_i$ must first be undistorted. We use the one-parameter division model to parameterize the radial lens distortion [7], which has the form

$$f(\tilde{\mathbf{x}}_i, \lambda) = (\tilde{x}_i, \tilde{y}_i, 1 + \lambda(\tilde{x}_i^2 + \tilde{y}_i^2))^\top, \quad (3)$$

where the center of distortion is given; *i.e.*, \tilde{x}_i, \tilde{y}_i are the center-subtracted measurements from a feature detector.

In this work we incorporate constraints induced by a conjugate translation as derived in (2) with the one-parameter division model in (3) to achieve accurate affine rectification of imaged scene-planes from lens-distorted cameras. The homogeneous expression for lens distortion in (3) enables the relation for conjugate translations to be directly augmented to model lens distortion,

$$\alpha_i f(\tilde{\mathbf{x}}'_i, \lambda) = \mathbf{H}_u f(\tilde{\mathbf{x}}_i, \lambda) = [\mathbf{I}_3 + s_i^u \mathbf{u} \mathbf{l}^\top] \cdot f(\tilde{\mathbf{x}}_i, \lambda), \quad (4)$$

where α_i is some scalar, and $\tilde{\mathbf{x}}_i \leftrightarrow \tilde{\mathbf{x}}'_i$ is the point correspondence.

3. Solvers for distorted conjugate translations

The model for radially-distorted conjugate translations in (4) defines the unknown geometric quantities: (i) division-model parameter λ , (ii) scene-plane vanishing line

$\mathbf{l} = (l_1, l_2, l_3)^\top$, (iii) vanishing translation direction $\mathbf{u} = (u_1, u_2, u_3)^\top$ (see Sec. 3.2 for the two-direction extensions), (iv) scale of translation s_i^u for correspondence $\tilde{\mathbf{x}}_i \leftrightarrow \tilde{\mathbf{x}}'_i$, (v) and the scalar parameter α_i .

The solution for \mathbf{l} is constrained to the the affine subspace $l_3 = 1$ of the real-projective plane, making it unique. This inhomogenous choice of \mathbf{l} is unable to represent imaged scene planes whose vanishing line passes through the origin of the image coordinate system (equivalently, the pencil of vanishing lines that meet the image origin). The degeneracy can be avoided by a transforming the image coordinate system so that the origin is the centroid of the measurements. The vanishing line cannot meet the convex hull of the points that are used to estimate it [4].

The vanishing direction \mathbf{u} must meet the vanishing line \mathbf{l} , which defines a subspace of solutions for \mathbf{u} . The magnitude of \mathbf{u} is set to the translation scale s_1^u of the first correspondence, which defines a unique solution

$$\mathbf{l}^\top \mathbf{u} = l_1 u_1 + l_2 u_2 + u_3 = 0 \quad \wedge \quad \|\mathbf{u}\| = s_1^u. \quad (5)$$

The relative scale of translation \bar{s}_i^u for each correspondence $\tilde{\mathbf{x}}_i \leftrightarrow \tilde{\mathbf{x}}'_i$ with respect to the magnitude of $\|\mathbf{u}\|$ is defined so that $\bar{s}_i^u = s_i^u / \|\mathbf{u}\|$. Note that $\bar{s}_1^u = 1$.

In this paper we propose four different minimal solvers for different variants of the problem of radially-distorted conjugate translations based on different translation directions and relative scales \bar{s}_i^u . These variants are motivated by features used to extract point correspondences.

Each affine-covariant feature defines an affine frame, *i.e.* an ordered triplet of points. Thus, 1 affine-frame correspondence provides the 3 point correspondences that translate in the same direction with the same scale. This is sufficient input for the one-directional solvers. In the case of similarity-covariant features, such as DoG [14], only a similarity frame can be constructed. A correspondence of similarity frames gives 2 point correspondences that translate jointly. Two correspondences of similarity-covariant features of different direction of the translation provide sufficient constraints for the two directional solvers.

Two *one-direction solvers* are proposed, which require 3 (2.5) coplanar point correspondences that translate in the same direction. The “3-point” solver $\text{H3l}u\mathbf{s}_u\lambda$ assumes that two of the point correspondences have the same scale of translation (*i.e.* $\bar{s}_1^u = \bar{s}_2^u = 1$), and the third point correspondence has an unknown relative scale of the translation \bar{s}_3^u . The “2.5-point” solver $\text{H2.5l}u\lambda$ assumes that all 3 point correspondences have the same relative scales of translation, *i.e.* $\bar{s}_1^u = \bar{s}_2^u = \bar{s}_3^u = 1$.

In addition, two *two-direction solvers* are proposed, which require 4 (3.5) coplanar point correspondences, 2 of which translate in one-direction \mathbf{u} and the remaining 2 in a different direction \mathbf{v} . Here the “4-point” solver $\text{H4l}u\mathbf{v}\mathbf{s}_v\lambda$ assumes that the first two point correspondences translate

in the direction \mathbf{u} with the same relative scale of translation, i.e., $\bar{s}_1^{\mathbf{u}} = \bar{s}_2^{\mathbf{u}} = 1$. The remaining two point correspondences translate in the direction \mathbf{v} with arbitrary translation magnitudes, i.e., the relative scales of translations of these two correspondences with respect to $\|\mathbf{v}\| = s_3^{\mathbf{v}}$ are $\bar{s}_3^{\mathbf{v}} = 1$ and an unknown relative scale $\bar{s}_4^{\mathbf{v}}$.

The “3.5-point” H3.5luv λ solver assumes that the relative scales $\bar{s}_1^{\mathbf{u}} = \bar{s}_2^{\mathbf{u}} = 1$ with respect to $\|\mathbf{u}\| = s_1^{\mathbf{u}}$ and $\bar{s}_3^{\mathbf{v}} = \bar{s}_4^{\mathbf{v}} = 1$ with respect to $\|\mathbf{v}\| = s_3^{\mathbf{v}}$.

In all proposed solver the scalar values α_i are eliminated from (4). This is done by multiplying (4) by the skew-symmetric matrix $[f(\tilde{\mathbf{x}}'_i, \lambda)]_{\times}$. The fact that the join of a point \mathbf{x}_i with itself $[\mathbf{x}_i]_{\times} \mathbf{x}_i$ is $\mathbf{0}$ gives,

$$\begin{bmatrix} 0 & -\tilde{w}'_i & \tilde{y}'_i \\ \tilde{w}'_i & 0 & -\tilde{x}'_i \\ -\tilde{y}'_i & \tilde{x}'_i & 0 \end{bmatrix} \times \begin{bmatrix} 1 + \bar{s}_i^{\mathbf{u}} u_1 l_1 & \bar{s}_i^{\mathbf{u}} u_1 l_2 & \bar{s}_i^{\mathbf{u}} u_1 \\ \bar{s}_i^{\mathbf{u}} u_2 l_1 & 1 + \bar{s}_i^{\mathbf{u}} u_2 l_2 & \bar{s}_i^{\mathbf{u}} u_2 \\ \bar{s}_i^{\mathbf{u}} u_3 l_1 & \bar{s}_i^{\mathbf{u}} u_3 l_2 & 1 + \bar{s}_i^{\mathbf{u}} u_3 \end{bmatrix} \begin{pmatrix} \tilde{x}_i \\ \tilde{y}_i \\ \tilde{w}_i \end{pmatrix} = \mathbf{0}, \quad (6)$$

where $\tilde{w}_i = 1 + \lambda(\tilde{x}_i^2 + \tilde{y}_i^2)$ and $\tilde{w}'_i = 1 + \lambda(\tilde{x}'_i^2 + \tilde{y}'_i^2)$. The matrix equation in (6) contains three polynomial equations from which only two are linearly independent, since the skew-symmetric matrix $[f(\tilde{\mathbf{x}}'_i, \lambda)]_{\times}$ is rank two.

To solve the systems of polynomial equations resulting from the presented problems, we use the Gröbner basis method [6]. To generate efficient solvers we used the automatic generator of Gröbner basis solvers proposed in [10, 12]. However, for our problems the coefficients of the input equations are not fully independent. This means that using the default settings for the automatic generator [10, 12] that initialize the coefficients of equations by random values from \mathbb{Z}_p does not lead to correct solvers. To obtain working Gröbner basis solvers, one has to create correct problems instances with values from \mathbb{Z}_p for the automatic generator initialization.

Unfortunately, a straightforward application of the automatic generator [10, 12] to the needed constraints with correct coefficients from \mathbb{Z}_p resulted in large templates and unstable solvers, especially for the two-direction problems. The Gröbner basis solvers generated for the original constraints have template matrices with sizes 80×84 , 74×76 , 348×354 , and 730×734 for the H2.5lu λ , H3lu $s_{\mathbf{u}}\lambda$, H3.5luv λ and H4luv $s_{\mathbf{v}}\lambda$ problem respectively.

Therefore, we use a hidden-variable trick [6] with ideal saturation [13] to reformulate the constraints so that the solvers generated by the Gröbner basis method are smaller and stable. Using the hidden-variable trick we are able to eliminate unknowns that correspond to the vanishing translation directions, which results in simpler systems in only three or four unknowns. Next, we describe the solvers based on the hidden-variable trick in more detail.

3.1. One-direction solvers

For the “3-point” one-direction H3lu $s_{\mathbf{u}}\lambda$ solver we have $\bar{s}_1^{\mathbf{u}} = \bar{s}_2^{\mathbf{u}} = 1$. Therefore the constraints (6) result in two pairs of linearly independent equations without the scale parameter $\bar{s}_i^{\mathbf{u}}$ for $i = 1, 2$, and two linearly independent equations with an unknown relative scale $\bar{s}_3^{\mathbf{u}}$ for the third point correspondence, i.e., $i = 3$. Additionally, we have a constraint (5). All together we have seven equations in seven unknowns $(l_1, l_2, u_1, u_2, u_3, \bar{s}_3^{\mathbf{u}}, \lambda)$.

Note, that these equations are linear with respect to the vanishing translation direction \mathbf{u} . Therefore, we can rewrite the seven equations as

$$\mathbf{M}(l_1, l_2, \bar{s}_3^{\mathbf{u}}, \lambda) \begin{pmatrix} u_1 \\ u_2 \\ u_3 \\ 1 \end{pmatrix} = \mathbf{0} \quad (7)$$

where $\mathbf{M}(l_1, l_2, \bar{s}_3^{\mathbf{u}}, \lambda)$ is a 7×4 matrix which elements are polynomials in $(l_1, l_2, \bar{s}_3^{\mathbf{u}}, \lambda)$.

Since $\mathbf{M}(l_1, l_2, \bar{s}_3^{\mathbf{u}}, \lambda)$ has a null vector, it must be rank deficient. Therefore, all the 4×4 sub-determinants of $\mathbf{M}(l_1, l_2, \bar{s}_3^{\mathbf{u}}, \lambda)$ must equal zero. This results in $\binom{7}{4} = 35$ polynomial equations which only involve four unknowns.

Unfortunately, the formulation (7) introduces a one-dimensional family of false solutions. These are not present in the original system and corresponds to solutions where the first three columns of \mathbf{M} become rank deficient. In this case there exist null vectors to \mathbf{M} where the last element of the vector is zero, i.e. not on the same form as in (7).

These false solutions can be removed by saturating any of the 3×3 sub-determinants from the first three columns of \mathbf{M} . The matrix \mathbf{M} has the following form,

$$\mathbf{M}(l_1, l_2, \bar{s}_3^{\mathbf{u}}, \lambda) = \begin{bmatrix} m_{11} & m_{12} & 0 & m_{14} \\ m_{21} & m_{22} & 0 & m_{24} \\ m_{31} & 0 & m_{33} & m_{34} \\ m_{41} & 0 & m_{43} & m_{44} \\ m_{51} & m_{52} & 0 & m_{54} \\ m_{61} & 0 & m_{63} & m_{64} \\ l_1 & l_2 & 1 & 0 \end{bmatrix} \quad (8)$$

where m_{ij} are polynomials in $l_1, l_2, \bar{s}_3^{\mathbf{u}}$ and λ . We choose to saturate the 3×3 sub-determinant corresponding to the first, second and last row since it reduces to only the top-left 2×2 sub-determinant, i.e. $m_{11}m_{22} - m_{12}m_{21}$, which is only a quadratic polynomial in the unknowns. The other 3×3 determinants are more complicated and leads to larger polynomial solvers. Using the saturation technique from Larsson *et al.* [13] we were able to create a polynomial solver for this saturated ideal. The size of the elimination template is 24×26 . Note that without using the hidden-variable trick the elimination template was 74×76 .

For the H2.5lu λ solver we can use the same hidden-variable trick. In this case $\bar{s}_1^{\mathbf{u}} = \bar{s}_2^{\mathbf{u}} = \bar{s}_3^{\mathbf{u}} = 1$ and therefore

the matrix M in (7) contains only three unknowns l_1, l_2 and λ . The minimal number of point correspondences necessary to solve this problem is 2.5. Therefore, for this problem we can drop one of the equations from (6), e.g., for $i = 3$, and the matrix M in (7) has size 6×4 . In this case all 4×4 sub-determinants of M result in 15 equations in 3 unknowns.

Similar to the 3 point case, this introduces a one-dimensional family of false solutions. The matrix M has a similar structure as in (8) and again it is sufficient to saturate top-left 2×2 sub-determinant. For this formulation we were able to create a solver with template size 14×18 (compared with 80×84 without using hidden-variable trick)

3.2. Two-direction solvers

In the case of the two-direction $H4luvs_v\lambda$ solvers, the input equations for two vanishing translation directions $\mathbf{u} = (u_1, u_2, u_3)^\top$ and $\mathbf{v} = (v_1, v_2, v_3)^\top$ can be separated into two sets of equations, i.e., the equations containing \mathbf{u} and the equations containing \mathbf{v} . Note that in this case we have two equations of the form (5), i.e., the equation for the direction \mathbf{u} and the equation for the direction \mathbf{v} and we have an unknown relative scale \bar{s}_4^v . Therefore, the final system of 10 equations in 10 unknowns can be rewritten using two matrix equations as

$$M_1(l_1, l_2, \lambda) \begin{pmatrix} u_1 \\ u_2 \\ u_3 \\ 1 \end{pmatrix} = \mathbf{0}, \quad M_2(l_1, l_2, \bar{s}_4^v, \lambda) \begin{pmatrix} v_1 \\ v_2 \\ v_3 \\ 1 \end{pmatrix} = \mathbf{0} \quad (9)$$

where M_1 and M_2 are 5×4 matrices where the elements are polynomials in (l_1, l_2, λ) and $(l_1, l_2, \bar{s}_4^v, \lambda)$ respectively.

Again all 4×4 sub-determinants of M_1 and M_2 must concurrently equal zero. This results in $5 + 5 = 10$ polynomial equations in four unknowns $(l_1, l_2, \bar{s}_4^v, \lambda)$. In this case, only 39 additional false solutions arise from the hidden-variable trick. The matrices M_1 and M_2 have a similar structure as in (8) and again it is sufficient to saturate the top-left 2×2 sub-determinants to remove the extra solutions. By saturating these determinants we were able to create a solver with template size 76×80 (previously 730×734).

Finally, for the “3.5-point” two-direction $H3.5luv\lambda$ solver $\bar{s}_1^u = \bar{s}_2^u = 1$ and $\bar{s}_3^v = \bar{s}_4^v = 1$ so we can drop one of the equations from the constraint (6), e.g., for $i = 4$. Therefore, the matrix M_2 from (9) has size 4×4 and it contains only 3 unknowns (l_1, l_2, λ) . In this case all 4×4 sub-determinants of M_1 and M_2 result in $5 + 1 = 6$ polynomial equations in three unknowns (l_1, l_2, λ) .

For this case we get 18 additional false solutions. Investigations in Macaulay2 [8] revealed that for this particular formulation it was sufficient to only saturate the top-left 2×2 sub-determinant of M_1 and the top-left element of M_2 . Saturating these we were able to create a polynomial solver with a template size of 54×60 (previously 348×354).

4. Implementation details

Details of the implementation used in the experiments are given in this section.

4.1. Features and descriptors

Affine-covariant feature detectors are highly repeatable on the same imaged scene texture with respect to significant changes of viewpoint and illumination [17]. Their proven robustness in the multi-view matching task makes them good candidates for representing the local geometry of repeated textures. In particular, for the experiments in Sec. 5 we use the Maximally-Stable Extremal Region and Hessian-Affine detectors [16, 18]. The detections are parameterized by 3 distinct points, which define an affine frame in the image space [19]. The image patch local to the affine frame is embedded into a descriptor vector by the RootSIFT transform [3, 14].

4.2. Appearance clustering

Affine frames are labeled as repeated texture by their appearance. The appearance of an affine frame is given by the RootSIFT embedding of the image patch local to the affine frame. The RootSIFT descriptors are agglomeratively clustered, which establishes pair-wise tentative correspondences among connected components. Each appearance cluster has some proportion of its indices corresponding to affine frames that represent the same repeated scene content, which are the *inliers* of that appearance cluster. The remaining affine frames are the *outliers*.

4.3. Robust estimation

The final models are estimated in a LO-RANSAC [5] framework. Samples for the minimal solvers are pairs of affine frames, each pair drawn from an appearance cluster. Each pair of affine frames across all appearance clusters has an equal probability of being drawn. The consensus is measured by the number of consistent pairs of affine frames within appearance groups, normalized by the size of each respective group. A non-linear optimizer following [20] is used as the local optimization step.

5. Experiments

The stabilities and noise sensitivities of the proposed solvers are evaluated on synthetic data. We compare the proposed solvers to a bench of four state-of-the-art solvers (also see Table 1). Included are two single-view solvers: $H2lu$ [22], which also incorporates constraints from conjugate translations, and $H4l\gamma$ [4], which solves directly for rectification and scale change. Also included are two full-homography and radial distortion solvers, $H5\lambda$ [7] and $H5\lambda_1\lambda_2$ [11], which we use for conjugate translation and lens distortion estimation.

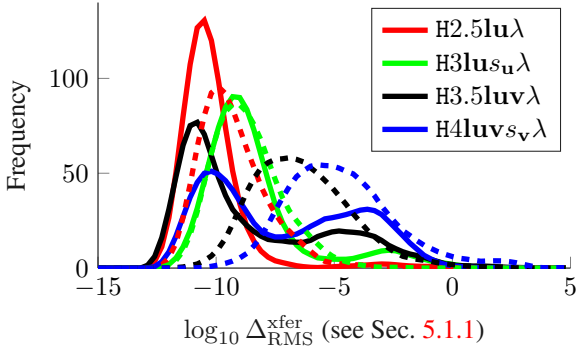


Figure 3: *Stability study*. Solvers with the hidden-variable trick are solid histograms; solvers without are dashed histograms. The \log_{10} transfer error is reported. The hidden-variable trick increases the stability of the proposed solvers.

5.1. Synthetic Data

The performance of the proposed solvers on 1000 synthetic images of 3D scenes with known ground-truth parameters is evaluated. A camera with a random but realistic focal length is randomly oriented and positioned with respect to a 10x10 square meter scene plane such that the plane is mostly in the camera’s field-of-view. Image resolution is set to 1000x1000 pixels. Conjugately translated affine frames are generated on the scene plane such that their scale with respect to the scene plane is realistic. This modeling choice reflects the use of affine covariant feature detectors for real images. The conjugately translated features are distorted according to the division model, and, for the sensitivity experiments, isotropic white noise is added to the distorted affine frames at increasing levels. Performance is characterized by the relative error of the estimated distortion parameter and by the transfer and warp errors, which measure the accuracies of the estimated conjugate translation and rectification (see Sec. 5.1.1 - 5.1.4).

5.1.1 Transfer error

We propose a geometric transfer error that jointly measures the accuracy of an estimated conjugate translation $\hat{\mathbf{h}}_{\mathbf{u}}$ and division model parameter $\hat{\lambda}$. The scene plane is tessellated by a 10x10 square grid of points $\{\mathbf{X}_i\}$. Let the translation on the scene plane induced by the noiseless pre-images of the point correspondences used to estimate $\hat{\mathbf{h}}_{\mathbf{u}}$ and $\hat{\lambda}$ be \mathbf{t} . Then the grid points are translated by $\mathbf{t}/\|\mathbf{t}\|$ to $\{\mathbf{X}'_i\}$. The grid and its translation are imaged by the ground-truth lens-distorted camera parameterized by matrix \mathbf{P} and division-model parameter λ . The imaged grid is given by $\tilde{\mathbf{x}}_i = f^d(\mathbf{P}\mathbf{X}_i, \lambda)$ and the translated grid by $\tilde{\mathbf{x}}'_i = f^d(\mathbf{P}\mathbf{X}'_i, \lambda)$, where f^d is the function that transforms from pinhole points to radially-distorted points. Then

	H2lu	H2.5lu λ	H3lus $u\lambda$	H3.5luv λ	H4luvs $v\lambda$	H4l γ	H5 λ	H5 $\lambda_1\lambda_2$
Reference	[22]					[4]	[7]	[10]
Distortion		✓	✓	✓	✓	✓	✓	✓
H_{∞}	✓	✓	✓	✓	✓	✓		
# points	2	2.5	3	3.5	4	4	5	5
# solutions	1	4	2	6	4	1	18	5

Table 1: Properties of the proposed solvers (in grey) versus the state-of-the-art solvers.

the geometric transfer error is defined as

$$\Delta_i^{\text{xfer}} = d(f^d([\mathbf{I}_3 + \frac{1}{\|\mathbf{t}\|}(\hat{\mathbf{h}}_{\mathbf{u}} - \mathbf{I}_3)]f(\tilde{\mathbf{x}}_i, \hat{\lambda}_1), \hat{\lambda}_2), \tilde{\mathbf{x}}'_i), \quad (10)$$

where $d(\cdot, \cdot)$ is the Euclidean distance. With the exception of $H5\lambda_1\lambda_2$, the evaluated solvers have the constraint that $\hat{\lambda}_1 = \hat{\lambda}_2$ [11]. The root-mean-square of transfer errors $\Delta_{\text{RMS}}^{\text{xfer}}$ for correspondences $\{(\tilde{\mathbf{x}}_i, \tilde{\mathbf{x}}'_i)\}$ is reported. For two-direction solvers, the transfer error in the second direction is included in $\Delta_{\text{RMS}}^{\text{xfer}}$. The transfer error is used in the stability study, where the solvers are tested over varying division model parameters, and in the sensitivity study, where the solvers are tested over varying noise levels with fixed division model parameter. Note that solver $H4l\gamma$ of [4] does not estimate conjugate translations, so it is not reported. For more details on transfer error see supplementary material.

5.1.2 Numerical Stability

The stability study measures the RMS transfer error of solvers (see Sec. 5.1.1) for noiseless affine-frame correspondences across realistic scene and camera configurations generated as described in the introduction to Sec. 5.1. The ground-truth parameter of the division model λ is drawn uniformly at random from the interval $[-6, 0]$. For a reference, the division parameter of $\lambda = -4$ is typical for wide field-of-view cameras like the GoPro where the image is normalized by $\frac{1}{\text{width} + \text{height}}$. Fig. 3 reports the histogram of \log_{10} RMS transfer errors. For all new solvers we evaluate a solver generated from constraints derived with (solid histogram) and without (dashed histogram) the hidden-variable trick. The hidden-variable trick significantly improves the stability of the proposed solvers. The increased stabilities of the hidden-variable solvers most likely result from the reduced size of the G-J elimination problems needed by these solvers. The hidden-variable solvers are used going forward for the remainder of the experiments.

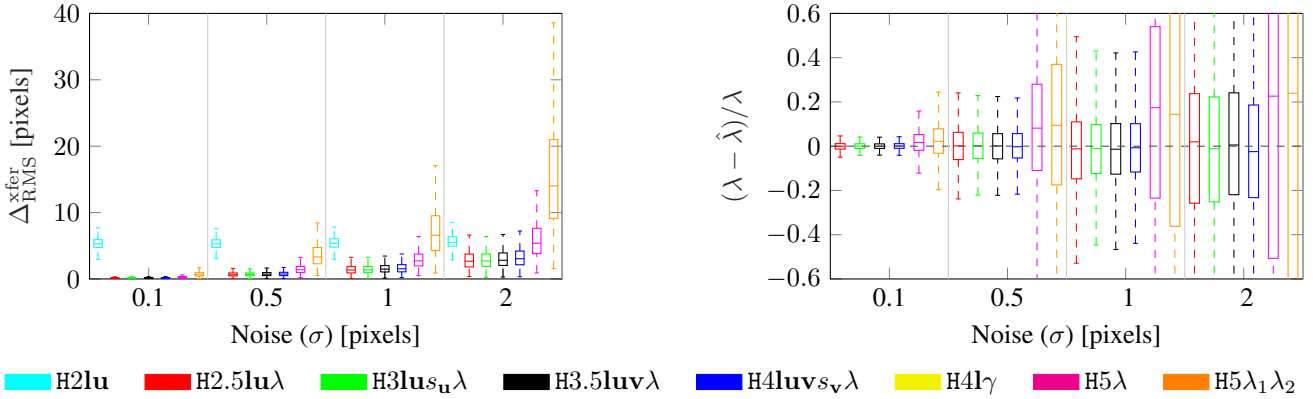


Figure 4: *Sensitivity studies*. Comparison of error after 25 iterations of a simple RANSAC for different solvers and increasing levels of white noise added to the affine correspondences, reporting $\Delta_{\text{RMS}}^{\text{xfer}}$ (left) and relative radial distortion error (right).

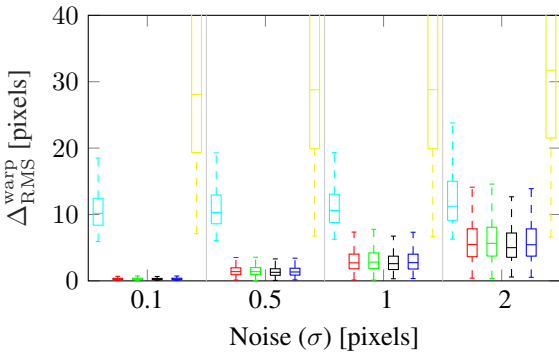


Figure 5: *Warp error*. Error comparison of different solvers after 25 iterations of a simple RANSAC for increasing levels of white noise added to the affine correspondences.

5.1.3 Noise Sensitivity

The proposed and state-of-the-art solvers are tested with increasing levels of white noise added to the affine correspondences induced by the ground-truth conjugate translation and lens distortion parameter. The white noise is parameterized by the standard-deviation of a zero-mean isotropic Gaussian distribution, and the solvers are tested at noise levels of $\sigma \in \{0.1, 0.5, 1, 2\}$. The ground truth division model parameter is set to $\lambda = -4$, which is typical for GoPro-type imagery. The solvers are wrapped in a simple RANSAC-loop, which minimizes the RMS transfer error $\Delta_{\text{RMS}}^{\text{xfer}}$ over 25 sampled affine-frame correspondences. Results are calculated from the estimate given by RANSAC and summarized for the 1000 generated scenes as boxplots. The interquartile range is contained within the extents of a box, and the median is the horizontal line dividing the box.

As shown in Fig. 4 the proposed solvers give the most accurate joint estimation of conjugate translation and di-

vision model parameter as measured by the RMS transfer error $\Delta_{\text{RMS}}^{\text{xfer}}$ and relative error of estimated division model parameter. As expected, the minimal parameterization of the radially-distorted conjugate translation solvers—H2.5lu λ , H3lus $u\lambda$, H3.5luv λ , H4luvs $v\lambda$ —show less sensitivity to noise than the overparameterized radially-distorted homography solvers H5 λ and H5 $\lambda_1\lambda_2$ for both measures. The standard conjugate translation solver H2lu shows significant bias (see the transfer error $\Delta_{\text{RMS}}^{\text{xfer}}$ boxplots) since it does not model radial lens distortion. All of the proposed solvers give a solution with less than 5 pixel RMS transfer error $\Delta_{\text{RMS}}^{\text{xfer}}$ and estimate the correct division model parameter at least half the time at the 2 pixel noise level with 25 iterations of RANSAC.

5.1.4 Warp error

Since the accuracy of scene-plane rectification is a primary concern, we also report the warp error for rectifying homographies proposed by Pritts *et al.* [21], which we augment with the division model for radial lens distortion. A rectifying homography H_∞ of an imaged scene plane is constructed from its vanishing line \mathbf{l} as

$$H_\infty = \begin{bmatrix} 1 & 0 & 0 \\ 0 & 1 & 0 \\ 0 & 0 & \mathbf{l}^\top \end{bmatrix}. \quad (11)$$

A round trip between the image space and rectified space is made by undistorting and rectifying imaged coplanar points by the estimated lens distortion $\hat{\lambda}$ and rectifying homography \hat{H}_∞ and then re-warping and distorting the rectified points into the image by a synthetic camera constructed from the ground-truth lens distortion λ and rectifying homography H_∞ . Ideally, the synthetic camera constructed from the truth would project the undistorted and rectified points onto the original points.

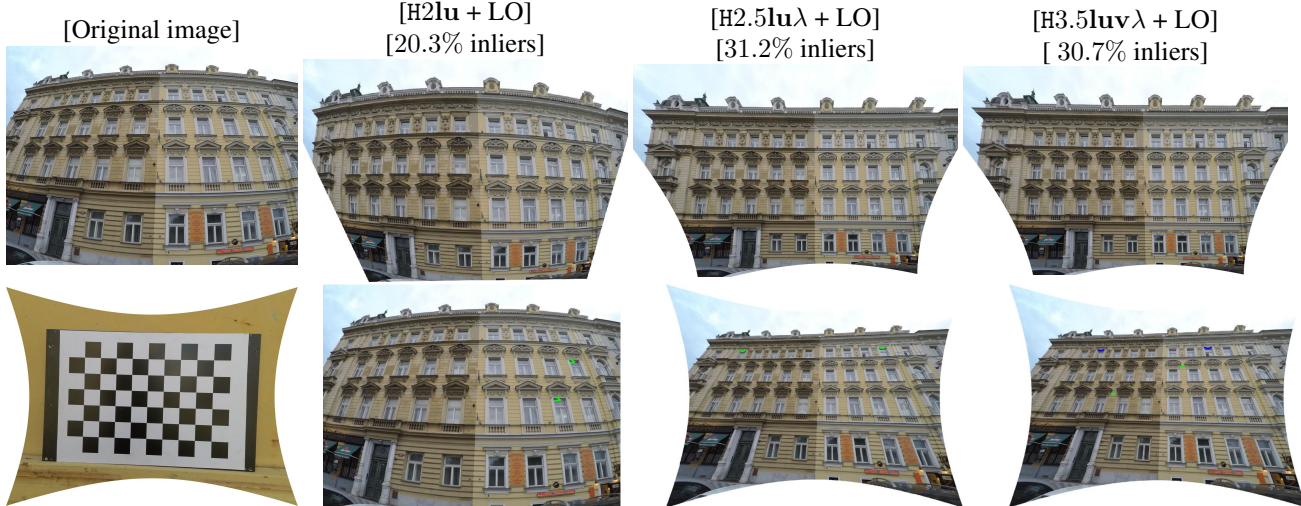


Figure 6: *GoPro Medium + different methods* (columns 2–4): The undistorted and rectified output of different methods (top row). Undistorted images by parameters estimated from a minimal samples (marked green and blue) (bottom row). Chessboard undistorted using parameters estimated by $H2.5lu\lambda + LO$ from the facade (bottom left).

Note that there is an affine ambiguity, denoted A , between \hat{H}_∞ and H_∞ , which is folded into the expression for the synthetic camera, namely $P(A) = (AH_\infty)^{-1}$, and estimated during computation of the warp error,

$$\Delta^{\text{warp}} = \min_{\hat{A}} \sum_i d^2(\tilde{x}_i, f^d(P(\hat{A})\hat{H}_\infty f(\tilde{x}_i, \hat{\lambda})), \hat{\lambda}), \quad (12)$$

where $d(\cdot, \cdot)$ is the Euclidean distance, and $\{\tilde{x}_i\}$ are the imaged grid points of the scene-plane tesselation as defined in Sec. 5.1.1. The root mean square warp error for $\{\tilde{x}_i\}$ is reported and denoted as $\Delta_{\text{RMS}}^{\text{warp}}$. Note that the vanishing line is not directly estimated by solvers $H5\lambda$ of [7] and $H5\lambda_1\lambda_2$ of [11], so they are not reported.

The proposed solvers— $H2.5lu\lambda$, $H3lu\mathbf{s}_u\lambda$, $H3.5luv\lambda$, $H4luv\mathbf{s}_v\lambda$ —estimate rectifications with less than 5 pixel RMS warp error $\Delta_{\text{RMS}}^{\text{warp}}$, even at the 2 pixel noise level, see Fig. 5. The need radial lens distortion modeling is shown by the biased fits for the solvers $H2lu$, $H4\gamma$.

5.2. Real Images

In the first experiment we tested the proposed solvers on real images with increasing amounts of radial distortion. Fig. 1 and 2 show results for images taken by a GoPro Hero4 camera with different field-of-view (FOV) settings. The amount of radial distortion increases with respect to the field-of-view setting, namely narrow, medium and wide. More imagery, including results for cameras with small radial distortion (mobile phone cameras) and fisheye 8mm lenses can be found in the supplementary material.

Fig. 6 shows some results from the second experiment in which we compare the performance of two of the pro-

posed solvers, $H2.5lu\lambda$ and $H3.5luv\lambda$, to $H2lu$ in a state-of-the-art local-optimization (LO) framework (see [5, 20]). The two proposed solvers accurately estimate the division-model parameter (see the chessboard in Fig. 6 as a reference) and give a good rectification, while the LO-variant using the $H2lu$ solver is unable to recover the lens distortion parameter. In fact, on several images that we tested, including the image from Fig. 6, local optimization failed completely when initialized from $H2lu$. For more results see the supplemental material.

6. Conclusions

In this paper we propose the first minimal solvers that jointly solve for the affine rectification of an imaged scene plane and a camera’s radial lens distortion from coplanar repeated patterns. The solvers are derived from constraints induced by conjugate translations of an imaged scene plane, which are integrated with the division model of radial distortion. We transformed the constraints to simplify the structure of the systems of polynomial equations, while explicitly accounting for the parasitic solutions that arose from the new formulation. The systems of polynomial equations induced from the constraints are solved using a method based on Gröbner bases. The proposed solvers are incorporated into a RANSAC-based estimator. Rectification and radial lens distortion are recovered from only one conjugately translated affine-covariant feature or two independently translated similarity-covariant features. Our experiments on synthetic and real images confirm that RANSAC quickly and reliably finds a model that accurately undistorts and rectifies, even for difficult scenes.

References

- [1] D. Aiger, D. Cohen-Or, and N. Mitra. Repetition maximization based texture rectification. *Computer Graphics Forum*, 31(2):439–448, 2012. 1
- [2] M. Antunes, J. P. Barreto, D. Aouada, and B. Ottersten. Unsupervised vanishing point detection and camera calibration from a single manhattan image with radial distortion. In *CVPR*, July 2017. 2
- [3] R. Arandjelović and A. Zisserman. Three things everyone should know to improve object retrieval. In *CVPR*, 2012. 5
- [4] O. Chum and J. Matas. Planar affine rectification from change of scale. In *ACCV*, 2010. 1, 2, 3, 5, 6
- [5] O. Chum, J. Matas, and v. Obdržálek. Enhancing RANSAC by generalized model optimization. In *ACCV*, 2004. 5, 8
- [6] D. Cox, J. Little, and O. D. Using algebraic geometry. Springer, 2004. 4
- [7] A. W. Fitzgibbon. Simultaneous linear estimation of multiple view geometry and lens distortion. In *CVPR*, 2001. 2, 3, 5, 6, 8, 12
- [8] D. R. Grayson and M. E. Stillman. Macaulay 2, a software system for research in algebraic geometry, 2002. 5
- [9] R. I. Hartley and A. W. Zisserman. *Multiple View Geometry in Computer Vision*. Cambridge University Press, ISBN: 0521540518, second edition, 2004. 1, 3
- [10] Z. Kukelova, M. Bujnak, and T. Pajdla. Automatic generator of minimal problem solvers. In *ECCV*, 2008. 2, 4, 6
- [11] Z. Kukelova, J. Heller, B. M., and T. Pajdla. Radial distortion homography. In *CVPR*, 2015. 1, 2, 5, 6, 8
- [12] V. Larsson, K. Åström, and M. Oskarsson. Efficient solvers for minimal problems by syzygy-based reduction. In *CVPR*, 2017. 2, 4
- [13] V. Larsson, K. Åström, and M. Oskarsson. Polynomial solvers for saturated ideals. In *ICCV*, 2017. 2, 4
- [14] D. Lowe. Distinctive image features from scale-invariant keypoints. *IJCV*, 60(2):91–110, 2004. 2, 3, 5
- [15] M. Lukáč, D. Sýkora, K. Sunkavalli, E. Shechtman, O. Jamriška, N. Carr, and T. Pajdla. Nautilus: Recovering regional symmetry transformations for image editing. *ACM Trans. Graph.*, 36(4):108:1–108:11, July 2017. 1
- [16] J. Matas, O. Chum, M. Urban, and T. Pajdla. Robust wide baseline stereo from maximally stable extremal regions. In *BMVC*, 2002. 2, 5
- [17] K. Mikolajczyk and C. Schmid. A performance evaluation of local descriptors. *PAMI*, 2004. 5
- [18] K. Mikolajczyk and C. Schmid. Scale and affine invariant interest point detectors. volume 60, 2004. 2, 5
- [19] Š. Obdržálek and J. Matas. Object recognition using local affine frames on distinguished regions. In *BMVC*, 2002. 5
- [20] J. Pritts, O. Chum, and J. Matas. Detection, rectification and segmentation of coplanar repeated patterns. In *2014 IEEE Conference on Computer Vision and Pattern Recognition*, 2014. 1, 2, 5, 8
- [21] J. Pritts, D. Rozumnyi, M. P. Kumar, and O. Chum. Coplanar repeats by energy minimization. In *BMVC*, 2016. 7
- [22] F. Schaffalitzky and A. Zisserman. Geometric grouping of repeated elements within images. In *BMVC*, 1998. 2, 3, 5, 6
- [23] A. Vedaldi and B. Fulkerson. VLFeat: An open and portable library of computer vision algorithms. <http://www.vlfeat.org/>, 2008. 2
- [24] H. Wildenauer and B. Micušík. Closed form solution for radial distortion estimation from a single vanishing point. In *BMVC*, 2013. 1, 2
- [25] C. Wu, J. M. Frahm, and M. Pollefeys. Repetition-based dense single-view reconstruction. In *CVPR*, 2011. 1
- [26] Z. Zhang, A. Ganesh, X. Liang, and Y. Ma. TILT: transform invariant low-rank textures. *IJCV*, 99(1):1–24, 2012. 1

Radially-Distorted Conjugate Translations

Supplementary Material

A. Transfer error

The scene plane is tessellated by 10x10 square grid of points, denoted $\{X_i\}$, with 1 meter spacing between adjacent points. Suppose that $\mathbf{y} \leftrightarrow \mathbf{y}'$ is an undistorted point correspondence induced by the conjugate translation $H_u = [I_3 + \mathbf{u}\mathbf{l}^\top]$ in the imaged scene plane (here we assume that $s_i^u = 1$ since we speak about an individual point correspondence).

Points $\{X_i\}$ are translated by 1 meter on the scene plane in the direction of translation induced by the preimage of point correspondence $\mathbf{y} \leftrightarrow \mathbf{y}'$ giving the translated grid $\{X'_i\}$. The purpose of constructing the grid and its translation is to uniformly cover the scene plane that the camera images in its field of view. In this way the accuracy of the conjugate translation and lens distortion parameter estimation can be measured across most of the image. The conjugate translation H_u is not used directly because the magnitude of translation may span the extent of the scene plane, so applying it to the tessellation would transform the grid out of the field of view.

Let the camera be parameterized by the camera matrix $P = (AH)^{-1}$ (see Sec. 5.1.4 for the camera matrix definition) mapping pointwise the scene plane Π to the imaged scene plane π and division model parameter λ . The preimages of the undistorted point correspondence $\mathbf{y} \leftrightarrow \mathbf{y}'$ in the scene-plane coordinate system is, respectively, $\beta\mathbf{Y} = P^{-1}\mathbf{y}$ and $\beta'\mathbf{Y}' = P^{-1}\mathbf{y}'$. The translation \mathbf{t} of the preimages in the scene plane coordinate system is $\mathbf{t} = \mathbf{Y} - \mathbf{Y}' = (t_x, t_y, 0)^\top$.

Then $\|\mathbf{t}\|$ is the magnitude of translation between the repeated scene elements in the scene-plane coordinate system. Denote the homogeneous translation matrix $T(\mathbf{t})$ to be the matrix constructed from \mathbf{t} as

$$T(\mathbf{t}) = \begin{bmatrix} 1 & 0 & t_x \\ 0 & 1 & t_y \\ 0 & 0 & 1 \end{bmatrix}. \quad (13)$$

Then the translation of the grid points by unit distance is given by $\mathbf{X}'_i = T(\mathbf{t}/\|\mathbf{t}\|)\mathbf{X}_i$. Recall from (1) that a conjugate translation has the form $PT(\cdot)P^{-1}$. Using (2), the conjugate translation of unit distance in the direction of point correspondences $\mathbf{y} \leftrightarrow \mathbf{y}'$ is

$$\begin{aligned} H_{u/\|\mathbf{t}\|} &= PI_3P^{-1} + P \begin{pmatrix} t_x/\|\mathbf{t}\| \\ t_y/\|\mathbf{t}\| \\ 1 \end{pmatrix} \left[P^{-\top} \begin{pmatrix} 0 \\ 0 \\ 1 \end{pmatrix} \right]^\top \\ &= [I_3 + \frac{\mathbf{u}}{\|\mathbf{t}\|}\mathbf{l}^\top]. \end{aligned} \quad (14)$$

The transformation $H_{u/\|\mathbf{t}\|}$ can be written in terms of the conjugate transformation H_u induced by the undistorted point correspondence $\mathbf{y} \leftrightarrow \mathbf{y}'$ as

$$\begin{aligned} I_3 + \frac{\mathbf{u}}{\|\mathbf{t}\|}\mathbf{l}^\top &= I_3 + \frac{1}{\|\mathbf{t}\|}[I_3 + \mathbf{u}\mathbf{l}^\top - I_3] \\ &= I_3 + \frac{1}{\|\mathbf{t}\|}[H_u - I_3]. \end{aligned} \quad (15)$$

The derivation of (15) gives the form of transformation used in the transfer error $\Delta_{\text{RMS}}^{\text{xfer}}$ defined in Sec. 5.1.1, which maps from the undistorted images of the grid $\{x_i\}$ to its translated correspondences $\{x'_i\}$.

B. Extended experiments

The extended real-data experiments in the following pages include (i) images from narrow field-of-view cameras that are typical for consumer cameras and standard mobile phones; the chosen images also demonstrates the methods effectiveness on diverse scene content, (ii) images for very wide field-of-view lenses (8mm and 12mm) (iii) and an additional local-optimization experiment on a GoPro-wide image, which demonstrates the need for a minimal solver that jointly estimates lens distortion with affine-rectification to achieve an accurate undistorted rectification.



Figure B.1: *Narrow field-of-view and diverse scene-content experiments.* The method works well where there is little or no radial lens distortion. This imagery is typical of consumer cameras and standard mobile phones. The images are diverse and contain unconventional scene content. (top row) Input images. (middle row) Undistorted images using $H2.5lu\lambda+LO$ (bottom row) Undistorted and rectified outputs.

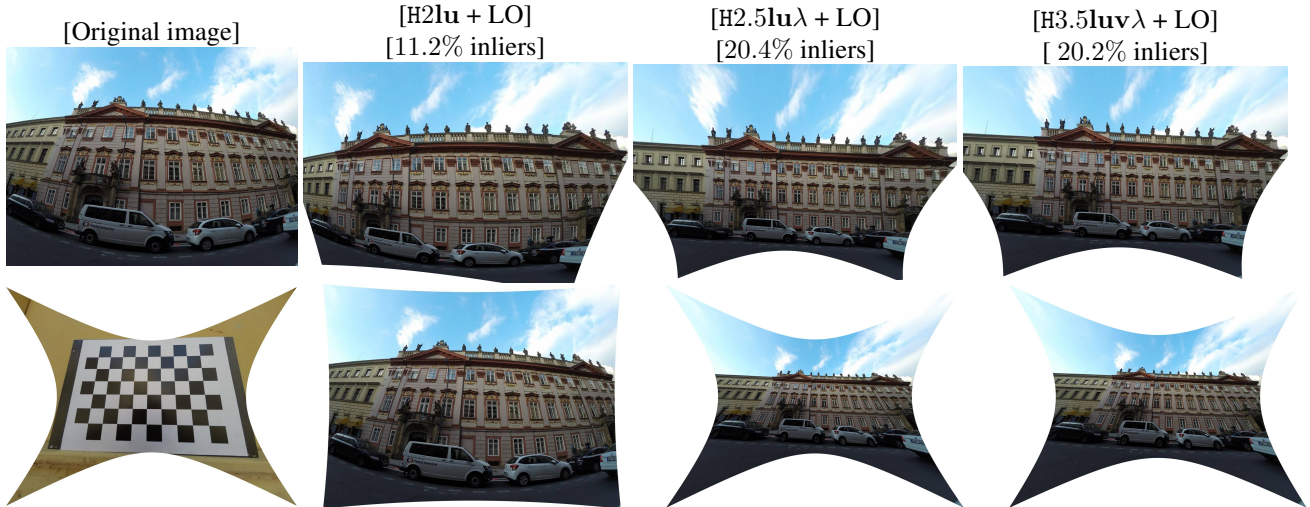


Figure B.2: *GoPro Wide + different methods* The results of local optimization are compared when inliers are chosen by the proposed solvers, which jointly solve for lens distortion ($H2.5lu\lambda$, $H3.5luv\lambda$), and a reference solver $H2lu$, which ignores lens distortion. It is clear that local optimization cannot recover from the biased selection of inliers chosen by $H2lu$, giving a poor solution. The result of the proposed solvers— $H2.5lu\lambda$, $H3.5luv\lambda$ —is much better. (columns 2–4): The undistorted and rectified output of different methods (top row). Undistorted images by parameters estimated from a minimal samples (bottom row). Chessboard undistorted using parameters estimated by $H2.5lu\lambda + LO$ from the facade (bottom left).

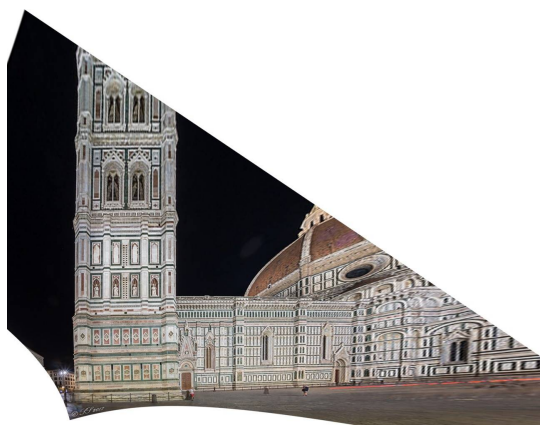
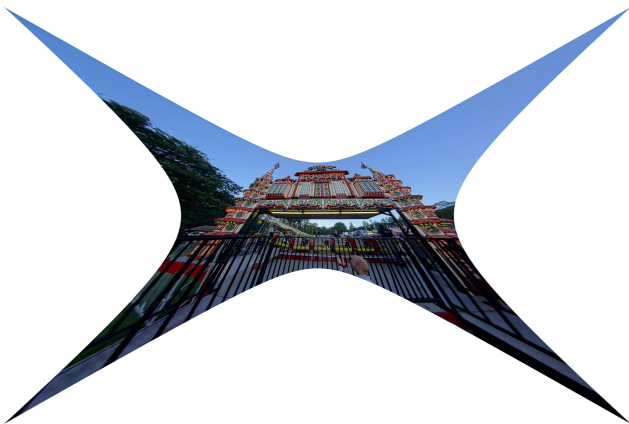


Figure B.3: *Very wide-angle cameras*. The proposed method is tested on imagery taken from 8mm and 12mm lenses. The division model used by [7] for radial lens distortion has only 1 parameter, which limits its use for modeling extreme lens distortion. Even so, the proposed method gives a reasonable solution for affine rectification, even though some radial distortion is visible. (top row) Input images: (left) 8mm lens, (right) 12mm lens. (middle row) Undistorted images using H2.5luλ + LO (bottom row) Undistorted and rectified results.



Figure B.4: *Problem Difficulty and method Robustness* (top left) The input to the method are ungrouped affine-covariant features. Common problems include missed detections of repeated texture, duplicate detections, and detections due to compression artifacts, all of which are visible in this example. (top right) The inliers respect to the number of all detected features can be a very small proportion. The method is sufficiently robust to estimate good undistortion (bottom left) and affine rectification (bottom right) even from a very sparse sampling of good affine-covariant features from the scene plane (top right).